Soft Matter

Cite this: *Soft Matter*, 2011, **7**, 3168

www.rsc.org/softmatter

**PAPER**

# Designing self-propelled microcapsules for pick-up and delivery of microscopic cargo

**German V. Kolmakov,[a] Victor V. Yashin,[a] Steven P. Levitan[b] and Anna C. Balazs*[a]**

***Received 25th August 2010, Accepted 13th December 2010***
**DOI: 10.1039/c0sm00864h**



Using computational modeling, we design a system of active polymeric microcapsules that pick-up, convey and drop-off a cargo between locations on a patterned surface. To create this system, we harness "signaling" and "target" capsules, which release nanoparticles into the surrounding solution. These nanoparticles bind to the underlying surface and thereby create adhesion gradients that trigger the spontaneous motion of the capsules. One signaling and two target capsules are found to form a stable triad, which can transport a cargo of four target capsules. Guided by an adhesive stripe on the surface, the triad and cargo form a "train" that moves autonomously along the substrate. The stripe is designed to encompass a small region with a lower adhesive strength. Through the aid of this patch, the triad can deposit its cargo and move on to potentially pick up a new payload at another location. Since the microcapsules can encase a wide variety of compounds, the system could provide an effective means of autonomously transporting a broad range of substances within microfluidic devices.

## I Introduction

A significant challenge in utilizing microfluidic devices for a range of applications is establishing effective means of transporting "cargo" through the microchannels.[1,2] In this context, cargo refers to nano- or micro-carriers filled with drugs or other chemicals that need to be picked-up, moved and dropped off at specific locations within the device so that a variety of assays or chemical syntheses can be performed. Using an applied light source, researchers demonstrated that living, unicellular algae could be directed to pick-up and deliver polymeric beads within microchannels.[2] In many situations, however, it is desirable to harness synthetic micro-carriers that can perform these pick-up and delivery chores autonomously, without the use of external stimuli. The recent advances in devising self-propelled nano- and micro-scale particles[1,3–7] can facilitate the development of such smart, active carriers for microfluidic applications. For example, we recently demonstrated that synthetic microcapsules can self-organize into a variety of autonomously moving structures.[7] The latter structures, however, did not move along a pre-specified path, so cargo could not be reliably or repeatedly delivered to a particular location within a device. Herein, we use computational modeling to design a system of "mini-mover" microcapsules that can collect and then convey other capsules to *specific locations* in a microchannel. All the capsules in this system are self-propelled; they move, in part, due to self-induced adhesion gradients that are dynamically formed on the underlying surface. The motion of these capsules is guided by micro-scale stripes, which can be readily introduced onto the surface through various lithographic means. As we show below, once the mini-mover has deposited its cargo, it can move on to potentially pick up a new payload at another location. Since the microcapsules can encase a wide variety of compounds, the system could provide an effective means of autonomously transporting a broad range of substances within micro-scale chambers.

In designing this system, we envision our fundamental structural units to be microcapsules fabricated by the sequential deposition of polyelectrolyes, using a technique referred to as the layer-by-layer (LbL) method,[8] or "polymersomes" fabricated from block copolymers.[9] The shells of these micro-carriers are sufficiently robust to act as a protective barrier, and adequately permeable for the controlled exchange of reagents with an external solution.[10] Furthermore, the permselectivity of the shells can be readily tuned.[11–15] By functionalizing the shell's outer surface, these capsules can bind to an underlying substrate.[11] Furthermore, the LbL microcapsules can encapsulate and controllably release various nanoparticles.[14–16] As we describe below, it is these attributes that make the microcapsules optimal materials for creating the "mini-movers".

In our computer simulations, we consider two types of active microcapsules, "signaling" and "target", which respectively release "agonists" and "antagonists" nanoparticles into the surrounding fluid. Our inspiration for these studies comes from cellular signaling processes, where dissolved agonists bind to the cell and promote the signaling process (production and release of the signal molecule), while antagonists that bind to the cell suppress these processes.[17] In our model, the agonist and

[a]*Chemical Engineering Department, University of Pittsburgh, Pittsburgh, PA, 15261, USA. E-mail: balazs@pitt.edu*
[b]*Electrical and Computer Engineering Department, University of Pittsburgh, Pittsburgh, PA, 15261, USA*

antagonist particles perform two functions: control the permeabilities of the capsules and alter the capsule–substrate interactions. Specifically, the permeabilities of both capsules (and hence, the particle release rates) depend on the local concentration of dissolved particles, so that the system exhibits a biomimetic feedback or self-regulating mechanism.[7] Additionally, the released particles can adsorb onto the underlying substrate and thereby modify the wetting properties of the substrate. The agonists make the surface more adhesive or "stickier" for the capsules, while the antagonists make the surface less sticky. The motion of the capsules is initiated by the release of agonists from the signaling capsule but then, as the capsules move and "communicate" through the release of both agonists and antagonists, the adhesion gradient on the surface dynamically changes and this evolution helps direct the capsules to aggregate into clusters that undergo sustained motion.

Below, we first briefly describe the computational model we used to capture these complex interactions among the capsules, the nanoparticles, the fluid and the underlying substrate. We then provide results that demonstrate the functionality of our autonomous mini-movers in picking up, transporting and dropping off cargo and subsequently, moving on to perform these functions at other locations. Our design of the above system is informed by a number of experimental studies that indicate that many of the necessary components are in place for creating this active assembly; these studies are discussed in Section IV. Our conclusions are given in Section V.

## II Methodology

We use our hybrid "LBM/LSM" approach[18–20] to simulate adaptive, three-dimensional capsules that are localized on the surface and immersed in a host fluid. The latter technique integrates the lattice Boltzmann model (LBM) for fluid dynamics with the lattice spring model (LSM) for the micromechanics of elastic solids. *Via* the LSM, the capsule's elastic, solid shell is constructed from a triangular lattice of harmonic springs that connect regularly spaced mass points, or nodes.[18–20] The spring forces $\boldsymbol{F}_s$ on node $\boldsymbol{r}_i$ is equal to

$$\boldsymbol{F}_s(\boldsymbol{r}_i) = -\sum_j k_j \left[\left(r_{ij} - r_{ij}^{eq}\right)\Big/ r_{ij}\right]\boldsymbol{r}_{ij} \qquad (1)$$

where the summation runs over all nearest- and next-nearest-neighbor nodes. The quantity $\boldsymbol{r}_{ij} = \boldsymbol{r}_i - \boldsymbol{r}_j$ is the radius vector between $i^{th}$ and $j^{th}$ nodes, $r_{ij}^{eq}$ is the equilibrium length of the spring and $k_j$ is the spring constant. The total force $\boldsymbol{F}$ acting on a node consists of the following: the sum of the spring forces between the masses (representing the elastic response of the solid shell), the force exerted by the fluid on the shell at the fluid–solid boundary, and the adhesion forces at the solid substrate (see below). To capture the dynamics of the solid shell, we numerically integrate Newton's equations of motion, $M(\mathrm{d}^2\boldsymbol{r}_i/\mathrm{d}t^2) = \boldsymbol{F}(\boldsymbol{r}_i)$, where $M$ is the mass of a node.

The capsule's spherical shell is formed from two concentric layers of LS nodes; each layer contains $N = 122$ nodes. These two layers are separated by a distance of $\Delta x_{LSM} = 1.5\Delta x$, where $\Delta x_{LSM}$ is the lattice spacing between nearest nodes in the LSM and $\Delta x$ is the spacing in the LBM (see below). The outer radius of the shell was taken to be $R = 5\Delta x$. Given that $k_1$ and $k_{\sqrt{2}}$ are respectively the spring constants in the orthogonal and the diagonal directions, then for $k_1/2 = k_{\sqrt{2}} \equiv k$ and for small deformations, the LSM system obeys linear elasticity theory[21,22] and results in a Young's modulus of $E = 5k_j/2\Delta x_{LSM}$.

The LBM can be viewed as an efficient solver for the Navier–Stokes equation.[23] This lattice-based model consists of two processes: the propagation of fluid "particles" to neighboring lattice sites, and the subsequent collisions between particles when they reach a site. The fluid particles are representative of mesoscopic portions of the liquid, and are described by a particle distribution function $f_i(\boldsymbol{r},t)$, which characterizes the mass density of fluid particles at a lattice node $\boldsymbol{r}$ and time $t$ propagating in the direction $i$ with a constant velocity $\boldsymbol{c}_i$. (The velocities $\boldsymbol{c}_i$ in the $i^{th}$ direction are chosen so that fluid particles propagate from one lattice site to the next in exactly one time step $\Delta t$.) The time evolution of these distribution functions is governed by a discretized Boltzmann equation.[23] In three-dimensional systems, the simulations involve a set of 19 particle velocity distribution functions at each node. The hydrodynamic quantities of interest are moments of the distribution function, *i.e.*, the mass density $\rho = \Sigma_i f_i$, the momentum density $\boldsymbol{j} = \rho\boldsymbol{u} = \Sigma_i \boldsymbol{c}_i f_i$, with $\boldsymbol{u}$ being the local fluid velocity, and the momentum flux $\Pi = \Sigma_i \boldsymbol{c}_i \boldsymbol{c}_i f_i$.

In our LBM/LSM simulations, the fluid and solid phases interact through appropriate boundary conditions.[24–26] In particular, lattice spring nodes that are situated at the solid–fluid interface impose their velocities on the surrounding fluids; the velocities are transmitted through a linked bounce-back rule[27] to those LBM distribution functions that intersect the moving solid boundary. In turn, LS nodes at the solid–fluid interface experience forces due to the fluid pressure and viscous stresses at that boundary. We calculate the latter force based on the momentum exchange between the LBM particle and solid boundary, and then distribute this quantity as a load to the neighboring LS nodes.

In addition to modeling the above fluid–structure interactions, we must take into account the presence of the nanoparticles in the system. In particular, the signaling capsule releases agonist nanoparticles and the target acts as a source for antagonist nanoparticles. To simulate the diffusion of the agonist and antagonist nanoparticles within the encapsulated and host fluid, we use a Brownian dynamics model for the particles.[28–30] The nanoparticle trajectories obey a stochastic differential equation

$$\mathrm{d}\,\boldsymbol{r}(t) = \boldsymbol{u}(\boldsymbol{r},t)\mathrm{d}t + \sqrt{2D_0}\,\mathrm{d}\boldsymbol{W}(t) \qquad (2)$$

where the first term describes the advection due to the local fluid velocity $\boldsymbol{u}(r,t)$ and the second term describes the particle's Brownian motion, with $D_0$ being the particle's diffusion coefficient and $\mathrm{d}\boldsymbol{W}(t)$ being the differential of a Weiner process with unit variance. We neglect backflow effects (*i.e.*, the impact of the particles motion on the flow field); the latter assumption is valid for submicron sized particles at relatively low concentrations. We also neglect the interactions between the particles. In other words, we consider the nanoparticles to be point-like tracers that are characterized by their diffusion coefficients. We use a first order Euler scheme method to solve eqn (2).[28] Note that an ensemble average of the particle trajectories computed from eqn (2) is equivalent to solving the convection–diffusion equation for the concentration of nanoparticles.[28,31,32]

When the agonists and antagonists in the external solution diffuse sufficiently close to the outer surface of the capsules (*i.e.*, within a distance of $1.5\Delta x$), these dissolved particles will modify the permeabilities of the capsules' shells (and, hence, the particle release rates). To capture the microcapsules' response to the variations in the concentration of agonist, $C^t$, and antagonist, $C^s$, we model the dependence of the permeability of the capsules' shells *via* the following smoothed step functions (see Fig. 1):[7]

$$P^s = \frac{1}{2}P^s_{max}\left(1 - \tanh\left(\frac{C^s - C_{thresh}}{\Delta C}\right)\right),$$
$$P^t = \frac{1}{2}P^t_{max}\left(1 + \tanh\left(\frac{C^t - C_{thresh}}{\Delta C}\right)\right). \quad (3)$$

Here $P^s_{max}$ and $P^t_{max}$ are the maximum permeabilities of the signaling and target capsules' shells, respectively. In the present simulations, the sharpness of the transition from a "dormant" state with zero permeability of the capsule's shells to an "active" state with maximum permeability was taken equal to $\Delta C = 0.1 \times C_{thresh}$. We also set the threshold concentration for this transition, $C_{thresh}$, equal for the signaling and target capsules.

The above expressions are used to specify the diffusion of nanoparticles through the capsule's shell; namely, the particle diffusion through a permeable shell was modeled by the same stochastic differential equation as within the fluid, but with a different diffusion coefficient. For the signaling capsules, the diffusion coefficient within the shell is taken to be $D^{sh}_{max}P^s(C^s)/P^s_{max}$, where $P^s(C^s)$ is the concentration-dependent permeability defined by eqn (3) and $D^{sh}_{max}$ is the maximum diffusion coefficient of the nanoparticles within the signaling capsule's shell. For the target capsules, the diffusion coefficient within the shell at various values of $\xi = P^t_{max}/P^s_{max}$ was calculated as $\xi D^{sh}_{max}P^t(C^t)/P^t_{max}$ and $P^t(C^t)$ is defined by eqn (3) (*i.e.*, the maximum diffusion coefficient within the target capsule's shell is $\xi$ times smaller than that within the signaling capsule's shell). In the simulations, the permeability is considered to be uniform over the surface of a capsule. We set $D^{sh}_{max} = 0.1D_0$ and the diffusion coefficient within the fluid was taken equal to $D_0 = 4 \times 10^{-2}\ \Delta x^2\Delta t^{-1}$ (with $\Delta x$ and $\Delta t$ being the respective LBM lattice spacing and time step).[28]

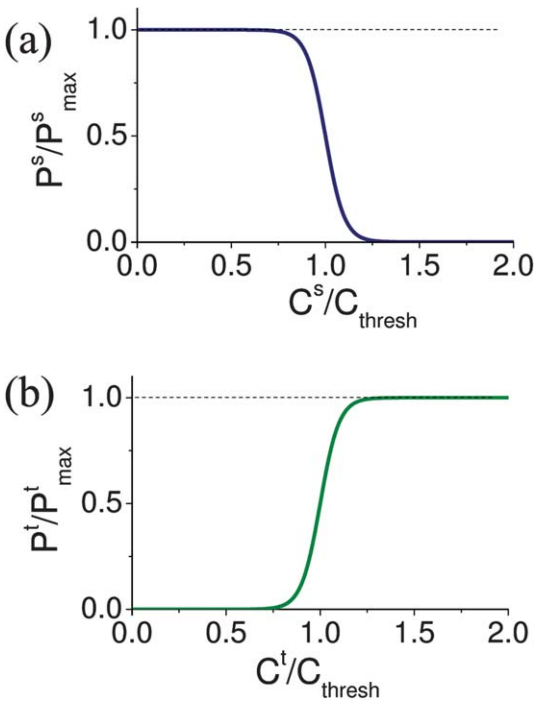


**Fig. 1** (a) Dependence of the permeability of the signaling capsule, $P^s$, on the concentration of antagonists, $C^s$, in the solution. $P^s$ is normalized by the maximum permeability of the signaling capsule and $C^s$ is normalized by the minimum concentration of antagonists in the solution that are necessary to affect the permeability of the capsule ($C_{thresh}$). (b) Dependence of the permeability of the target capsule, $P^t$, on the concentration of agonists $C^t$ in the solution. The values are normalized by the comparable parameters as in (a).

Each capsule in the simulation initially encases $N_p = 10^4$ nanoparticles. To model the fact that a capsule having a diameter of roughly 10 microns can enclose a very high number of nanoparticles, we assume that the nanoparticle concentration is not depleted during the time scale of our simulations. To this end, at each time step $\Delta t$, we add $\Delta N_p = 500 \times P$ nanoparticles to the interior of the capsules,[28] where $P$ is taken equal to $P^s$ for the signaling capsules and $P^t$ for the target capsules. (We do not add nanoparticles into dormant capsules, *i.e.*, when $P = 0$.)

Once the nanoparticles have diffused out of the capsules and into the surrounding solution, these species can bind to the surface and thereby modify the capsule–surface interaction.[4–7] We utilize the following Morse potential to capture the capsule–surface interaction:

$$\phi(r) = \varepsilon_s\left(1 - \exp\left[-\frac{(r - r_0)}{\kappa}\right]\right)^2 \quad (4)$$

where $\varepsilon_s$ and $\kappa$ characterize the respective strength and range of the interaction potential. The variable $r$ represents the distance between lattice nodes on the capsule's outer surface and the substrate, which is also composed of lattice nodes, and $r_0$ is the distance where this force equals zero. (Herein, we set $\kappa = 1$ and $r_0 = 1$.) In our simulations, diffusing agonists that bind to the surface increase the strength of the capsule–surface interaction and bound antagonists decrease this quantity. Thus, $\varepsilon_s$ is written as

$$\varepsilon_s = \varepsilon(1 - \theta + \theta') \quad (5)$$

where $\varepsilon$ is the adhesive strength of the bare surface, $\theta$ is the fractional coverage of the surface by the antagonists and $\theta'$ is the corresponding value for the agonists. Through dynamic variations in $\Delta\theta = \theta - \theta'$, the absorbing species create an adhesion gradient along the surface. If the gradient is sufficiently asymmetric, the capsules are driven by enthalpic forces to spontaneously move from a less adhesive to a more adhesive area.[4,7]

For a nanoparticle that does collide with the substrate, we assign a probability $w_{dep}$ that it is adsorbed onto this surface in a given time step $\Delta t$. The probabilities for antagonists, $w_{dep}$, and agonists, $w'_{dep}$, are proportional to the fraction of the empty surface sites:

$$w_{dep} = K_0\Delta t(1 - \theta),\ w'_{dep} = K_0\Delta t(1 - \theta') \quad (6)$$

Here, we set the reaction constants to be equal for both the agonists and antagonists, with $K_0 = 1/\Delta t$. When $\theta = 1$, all the

 

surface sites are occupied by nanoparticles, yielding a non-reactive substrate. We note that the adsorbed particles are immobile.

To calculate the fractional coverages $\theta$ and $\theta'$ at the substrate, this surface was divided into a number of cells, with each cell having an area of $\Delta x \times \Delta x$ (with $\Delta x$ being the LBM lattice spacing). The concentration of nanoparticles on the surface, $c_s = c(\boldsymbol{r},t)|_{surface}$, was calculated at the center of these cells. The maximum number of both agonist and antagonist nanoparticles that can adsorb onto a surface cell is controlled by the parameter $C_{max}$, which was held constant in all our simulations. Each surface cell can absorb up to $C_{max} = 100$ agonist and antagonist nanoparticles. (This number, in combination with the total number of nanoparticles at the onset of the simulations, was chosen to minimize the error in the results due to statistical fluctuations.[29]) The fractional coverage at a surface cell was computed as $\theta = c_s/C_{max}$, $\theta' = c'_s/C_{max}$, where values without and with primes correspond to antagonist and agonist nanoparticles, respectively. This behavior simulates the following general mass transfer boundary conditions for both agonists and antagonists[4,32]

$$-D_0 \boldsymbol{n} \nabla c|_{surface} = \mathrm{K}_0 c_s (1 - \theta) \quad (7)$$

with $D_0$ and $\boldsymbol{n}$ being the nanoparticle's diffusion coefficient in fluid and unit vector directed normal to the surface, respectively.

To direct the microcapsules' motion, we utilize a "sticky" stripe on the surface, which is drawn in green in the ensuing figures and has a width equal to the microcapsule diameter, $2R$. The signaling and target capsules experience different adhesive interactions with the stripe; the respective adhesive strengths are given by $\varepsilon^s$ and $\varepsilon^t$. (This behavior can be achieved experimentally if the signaling and target capsules are functionalized with different types of ligands.[33,34]) The adhesive interaction strength of the signaling capsule with the stripe was chosen to be $\varepsilon^s = 5\varepsilon$, where $\varepsilon$ is the adhesive strength on the bare surface outside the stripe. (We set the interaction strength with the bare surface equal for the signaling and target capsules.) We found that at lower values of $\varepsilon^s$, the adhesive interaction between the signaling capsule and the stripe was not sufficiently high for directing the microcapsules motion.

The sticky green stripe encompasses a blue patch and the target capsules experience a different adhesive interaction with the blue and green regions. Specifically, $\varepsilon^t = \varepsilon^t_b$ at $x_1 - \Delta x_s/2 < x < x_1 + \Delta x_s/2$, where $x_1$ is the $x$-coordinate of the center of the blue patch and the length of this blue patch is $\Delta x_s = 4R$. Within the green region, $\varepsilon^t = \varepsilon^t_g$. Below, we study the microcapsule motion at different values of $\varepsilon^t_b$ and $\varepsilon^t_g$.

Finally, we note that the size of the simulation box is equal to $L_x \times L_y \times L_z = 200 \times 200 \times 30(\Delta x)^3$. Furthermore, with respect to the nanoparticles, the top wall of the simulation box is assumed to be perfectly absorbing.

In the studies presented below, we focus on the motion of rigid capsules. Given that $V$ is the capsule velocity, and $\mu$ is the fluid viscosity, we specifically consider cases where both the dimensionless capillary number, $Ca = V\mu/E\Delta x_{LSM}$, and the capsule–surface interaction strength, $\Phi = \varepsilon N/E\Delta x_{LSM}\kappa^2$, are small and, hence, the capsules' shapes are close to spherical.[28] We set the interaction strength $\Phi = 10^{-2}$ and checked that in simulations $Ca \leq 10^{-4}$. (The effect that the mechanical deformation of the capsules' shells has on the behavior of the system will be considered in future studies.)

The capillary number represents the relative importance of the viscous stress in the surrounding fluid and the elastic stress in the capsule's shell. To put the above value of $Ca$ in context, we can consider LbL microcapsules that are propelled by an applied shear in a microchannel. We take the fluid to be an aqueous solution whose viscosity is $\mu \approx 10^{-3}$ kg s$^{-1}$ m$^{-1}$ and density is $\rho \approx 10^3$ kg m$^{-3}$. The elasticity of the microcapsule's shell is on the order of 0.1–1 GPa,[35–37] and these elastic properties are found to be independent of the speed of deformation.[37] (We note that the Young's modulus of the membrane can be tailored by varying the salt concentration in the solution,[38] or the solvent temperature.[39]) In typical flow experiments within a microchannel, the shear rate can be up to $\dot{\gamma} \approx 10^3$ to $10^4$ s$^{-1}$.[40] If we take experimentally realistic values of the membrane thickness $h$ to be about 50 nm for a 50 μm capsule,[36] we then obtain $Ca \approx 10^{-4}$, which is in the range considered in the simulations.

It is noteworthy that our model is also appropriate for modeling the interaction between leukocytes and a substrate. Leukocytes have a cytoskeleton that serves to maintain the spherical shape of the cell, and these cells have in fact been modeled as fluid-filled elastic shells. In the latter modeling studies, researchers typically use an effective membrane stiffness that lies in the range 0.01–0.3 N m$^{-1}$.[41–43] For leukocytes with radii of the order of 5 μm moving in an aqueous solution, one obtains typical values of the capillary number $Ca \approx 10^{-4}$, which is again in the range of our simulations.

The haptotactic motility of living cells is studied experimentally by measuring the velocity $\boldsymbol{v}_H$ of cell population migration on a surface having a gradient coating with some attractant, to which the cells bind reversibly.[44–46] It have been observed that

$$\boldsymbol{v}_H = H \nabla \frac{C}{k_d + C} \quad (8)$$

where $H$ is the haptotactic motility, $C$ is the attractant surface concentration, and $k_d$ is the dissociation constant of the cell–attractant bond. The experimentally determined value of $H$ depends on the type of cell and varies from $10^{-10}$ to $10^{-6}$ cm$^2$ s$^{-1}$.[44–46] In our simulations, we find the capsules' motility to be $H \approx 10^{-7}$ to $10^{-6}$ cm$^2$ s$^{-1}$ (given the microcapsule's diameter is 10 μm), which is comparable to that demonstrated by rolling leukocytes.[45] In the model, the motility of the capsules can be varied by changing the interaction strength $\varepsilon$ between the capsule and the substrate. The velocities of the capsules obtained in the simulations, $V \approx 0.2$ to 2 μm s$^{-1}$, are close to those observed in experiments on the haptotactic motion of vesicles surfing on a lipid bilayer, where the velocities are in the range of 1–5 μm s$^{-1}$.[47]

## III Results and discussion

Before describing the interactions among multiple capsules, we first discuss the nature of the self-regulating interaction between a signaling and a target capsule. Fig. 1 shows how the permeabilities of these capsules' shells, $P^s$ and $P^t$, depend on the local concentration of agonist and antagonist nanoparticles in the surrounding solution. The permeability of the signaling capsule's

shell is initially equal to $P^{s}_{max}$. At the onset of the simulation, agonist point particles are released from a source within the signaling capsule. The target capsule also has a permeable shell, and its permeability is initially characterized by $P^{t}_{min}$. When the concentration of diffusing agonists around the target capsule is higher than the threshold value $C^{t}_{thresh}$, the target releases antagonists, which also diffuse in the solution.

Eventually, the concentration of antagonists around the signaling capsule exceeds a critical threshold $C^{s}_{thresh}$; subsequently, the permeability of the signaling capsule decreases as shown in Fig. 1(a). Hence, the signaling capsule releases less agonist. The local concentration of the released agonists gradually decreases as these particles diffuse into the surrounding solution. When the concentration of agonists around the target capsule becomes lower than the threshold $C^{t}_{thresh}$, the permeability of the target capsule and, therefore, the release rate of the antagonists decrease (see eqn (3) and Fig. 1(b)). As the low concentration of released antagonists diffuses into the solution, their local concentration around the signaling capsule becomes lower than the threshold value $C^{s}_{thresh}$ and hence, the release of the agonists is no longer suppressed. In this manner, the system is effectively reset; with few antagonists in its vicinity, the permeability of the signaling capsule is again equal to $P^{s}_{max}$ and the above cycle is repeated. In previous studies, we found that this feedback mechanism, or adaptive behavior, is a necessary for achieving the cooperative motion of the capsules.[7]

In the following simulations, the ratio of the maximum permeabilities of the target and signaling capsules is fixed at $P^{t}_{max}/P^{s}_{max} = ¼$, and the threshold concentration of nanoparticles is set equal to $C_{thresh} = 12.5$ (particles/LBM lattice units); here, we set $C^{t}_{thresh} = C^{s}_{thresh} \equiv C_{thresh}$. With the latter values, the microcapsules form clusters or chains that undergo collective motion on a homogeneous substrate.[7]

Our fundamental "delivery device" is a triad composed of one signaling and two target microcapsules (see Fig. 2). In previous studies that did not involve an adhesive stripe, we found that this assembly forms a highly stable unit, which moves as a single entity over a range of $P^{t}_{max}/P^{s}_{max}$ and $C_{thresh}$ values.[7] In particular, we demonstrated that at $P^{t}_{max}/P^{s}_{max} = ¼$, a stable, moving triad is formed within a colony of microcapsules for values of $C_{thresh}$ that are in the range $5 \leq C_{thresh} \leq 15$. For the specific parameters considered here, the inset in Fig. 2(a) shows the trajectory that the center of mass of the triad makes on a homogeneous, adhesive surface. As is evident from this plot, the triad undergoes directed, linear motion.

To gain more insight into the mechanism that gives rise to the self-propelled motion of this triad, we plot two views of the adhesion gradients that these capsules create as they move on the homogenous, weakly adhesive substrate (see Fig. 2). To generate these plots, we calculate $\Delta\theta = \theta - \theta'$, the difference in the relative concentration of antagonists and agonists on the substrate, and the corresponding value of the adhesive interaction (see eqn (5)). Initially, the targets are located a finite distance from the signaling capsule (just as the capsules on the left in Fig. 3(a)); here, we set the initial distance between the centers of the signaling and target capsules to be $3.5R$. Agonists released from the signaling capsule make the substrate more adhesive; this can be seen as a potential well in Fig. 2(a) and the blue regions in Fig. 2(b). These bound agonists create a gradient that draws the

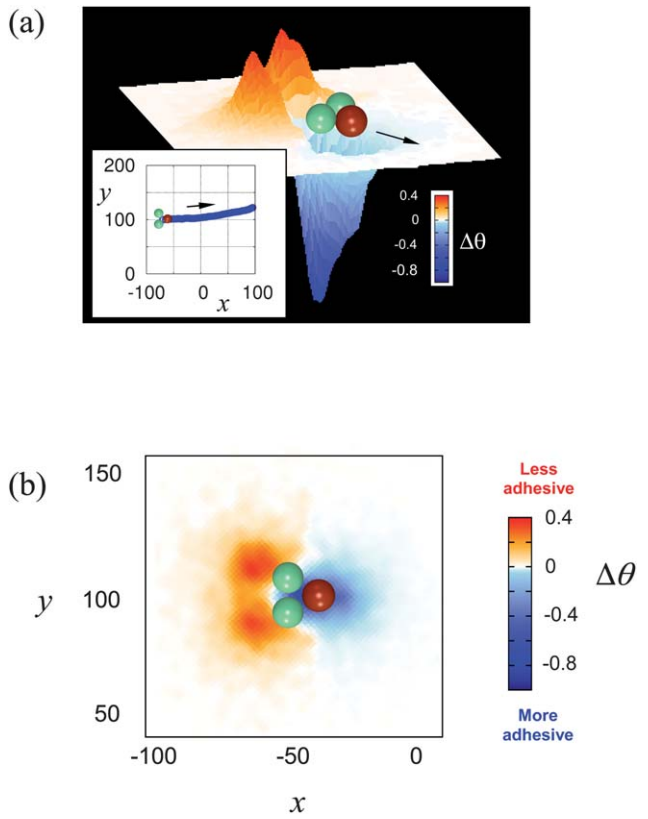


**Fig. 2** Two different views of the interactions between the triad and a homogeneously adhesive surface ($\varepsilon = 10^{-3}$) computed at $t = 300$. Time is normalized by the characteristic diffusion time $R^2/D_0$, where $R$ is the capsule radius and $D_0$ is the diffusion coefficient of the nanoparticles in solution. Spatial coordinates are measured in lattice Boltzmann units $\Delta x$. The parameter $\Delta\theta$ is the difference in the relative concentration of antagonists and agonists on the substrate. The color bar indicates the value of $\Delta\theta$; negative values correspond to more adhesive regions. (a) The adhesive strength $\varepsilon_s = \varepsilon(1 - \theta + \theta')$ is plotted as a topological map, with the peaks corresponding to less adhesive regions and hence, barriers to motion; the valleys correspond to more adhesion regions. Inset in (a): trajectory of the triad motion on the homogeneously adhesive surface; arrow indicates the direction of motion. (b) Top down view of the triad with the values of $\Delta\theta$ plotted around the capsule.

targets to the signaling unit. In this manner, the three capsules form a cluster.

Once the targets are sufficiently close to the signaling capsule, their permeabilities are affected by the agonists dissolved in the host solution (see Fig. 1) and hence, the targets are driven to release antagonists. Antagonists that bind to substrate make this surface less sticky; this is represented as the "bumps" in Fig. 2(a) and the yellow regions in Fig. 2(b). The presence of these less attractive regions prevents the triad from moving backwards (*i.e.*, to the left in Fig. 2). The latter behavior and the continued release of agonist from the signaling capsule, which creates the more adhesive regions ahead of the triad, drive the capsules to move forward (*i.e.*, to the right) as a coherent unit.

We now build on the above results to consider the scenario in Fig. 3(a), where the surface is decorated with a green adhesive stripe, which is more attractive to the capsules than the rest of the substrate. Furthermore, the stripe is relatively more attractive for

 

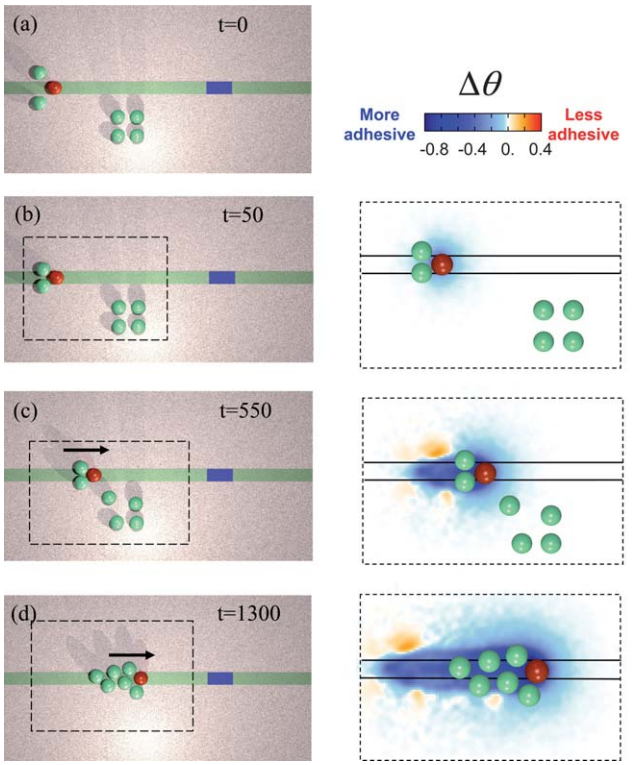


**Fig. 3** Left column: top down view of the formation and motion of a mobile train along the green adhesive stripe; the blue patch represents the less adhesive region. The signaling capsule is drawn in red and the target capsules are drawn in green. The blue patch is positioned at $x_1 = 60\Delta x$. Right column: changes in the adhesion strength on the surface in the regions marked by the dotted lines in the left frames.

the signaling capsules than the targets; the ratio of the adhesive strengths for the target and signaling capsules at the green portion of the stripe is set equal to $\varepsilon_g^t/\varepsilon^s = 2.5 \times 10^{-2}$. The three capsules on the left constitute the elements of our mini-mover and the group of four targets near the stripe constitute the cargo that must be picked-up. (Note that all of the target capsules are considered to be identical in these simulations.) At early times, we see that the three capsules cluster together to form the triad (for reasons described above). Due to the greater adhesion strength on the green path, the self-propelled triad moves autonomously along this stripe. Thus, the adhesive stripe allows one to control the movement of the microcapsules on the surface.

As the triad navigates the stripe, agonists emanating from the leading signaling capsule become bound to the surface (see Fig. 3(b)–(d)). The adsorbed agonists create an adhesion gradient, which makes the region near the cluster more attractive. Pulled by favorable enthalpic forces, the four capsules spontaneously move along the gradient, towards the more adhesive region. Drawn to the triad, the cluster comes in range of the stripe and due to the relatively strong attractive interaction between the capsules and this green stripe, the four-target cargo becomes localized on this band (see Fig. 3(d)). In effect, the triad has deposited a nanoparticle trail that leads the cargo onto the stripe.

Fig. 4 shows the movement of the cargo-laden triad along the adhesive stripe. Specifically, at time $t = 2200$, the system has self-organized into a long train that moves along the green band. The deposited agonists that emanate from the signaling capsule help maintain the integrity of the train. Hydrodynamic interactions are also critical for keeping this structure intact.[7]

As can be seen in these figures, the stripe contains a blue patch; the target capsules experience a weaker adhesive interaction with this blue patch than with the green stripe. Here, the ratio of the strength of the adhesive interaction for the targets on the blue and green regions is given by $\varepsilon_b^t/\varepsilon_g^t = 0.4$. The presence of this blue patch is important for the drop-off of the cargo. In particular, the green–blue interface forms a sharp adhesion gradient, and thus, presents a potential barrier for the capsules' motion. Due to their interaction with the barrier, the four-capsule cargo is arrested at the green–blue interface, as seen in Fig. 4(c). On the other hand, the difference between the adhesion strengths of the blue and green regions is not sufficient to stop the triad moving at the head of the train. As a consequence, the triad passes the blue region and continues its movement along the stripe (Fig. 4(c)).

To further elucidate why the motion of the four-capsule cargo is arrested while the triad continues to move, we calculate the profiles shown in Fig. 5. (In this simulation, we set $\varepsilon_g^t/\varepsilon^s = 2.5 \times 10^{-2}$ and $\varepsilon_b^t/\varepsilon^s = 10^{-2}$.) Fig. 5(a) shows the adhesion profile that arises from the deposition of the nanoparticles on the surface as the train of capsules moves along the stripe and interacts with the blue patch; the latter data are calculated using eqn (5). The specific position of the capsules with respective to this patch is indicated by the schematic image above Fig. 5(b).

Fig. 5(b) and (c) show $F_x^{adh}$, the $x$-component of the force acting on the capsules, as a function of $x$, the spatial coordinate directed horizontally along the stripe. The relative positions of the capsules at time $t = 4000$ (Fig. 5(b)) and 500 time steps later (Fig. 5(c)) are indicated by the schematic images above the respective plots. (Since the scale in the $x$ coordinate of the plots is not sufficiently fine, the capsule positions in the schematics are not exact, but rather serve to indicate the approximate location of the particles.) The blue curves depict the adhesive forces acting

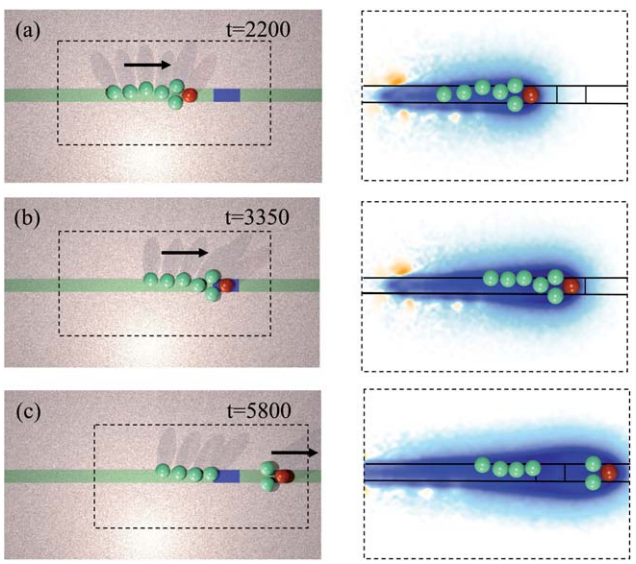


**Fig. 4** Continuation of Fig. 3: the four-capsule cargo is arrested at the blue patch on the stripe while the triad continues to move.

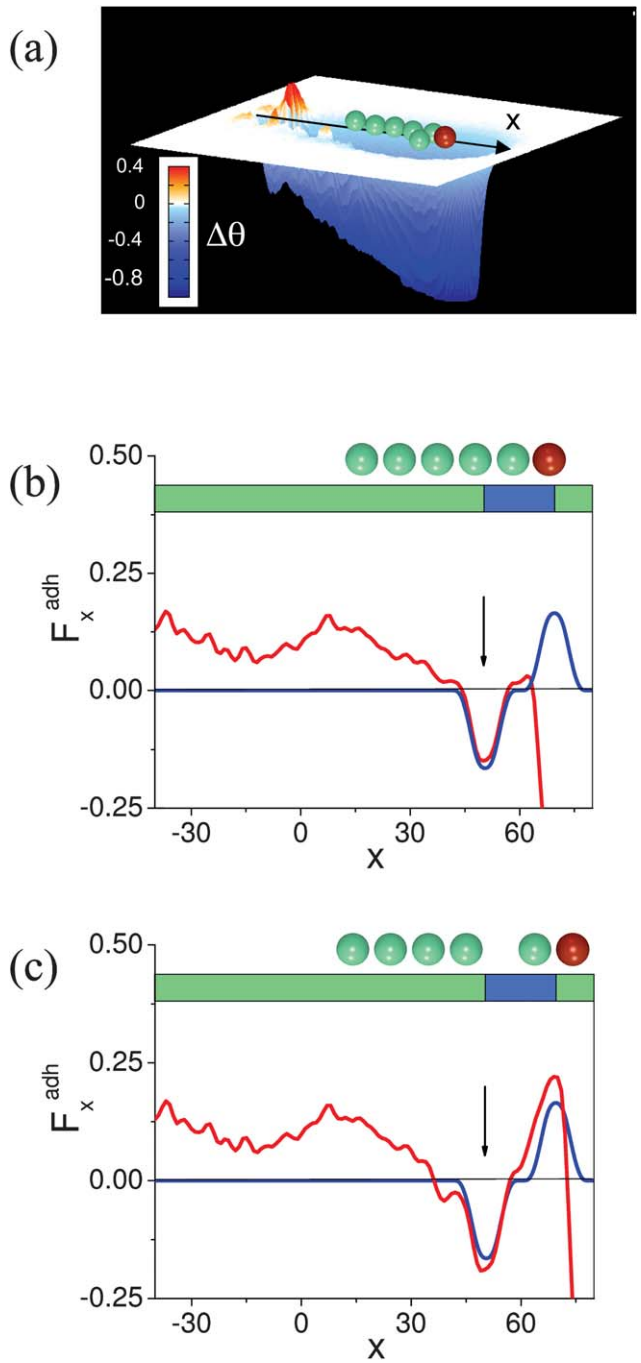


**Fig. 5** Adhesion profile and forces characterizing the interaction between the train (triad and four-capsule cargo) and the patterned surface. (a): Adhesion profile on the surface due to the deposited nanoparticles at time $t$ =4000. (b and c): The $x$-component of the adhesive force, $F_x^{adh}$, acting on the capsules at times $t$ = 4000 and $t$ = 4500, respectively; schematic images above (b) and (c) indicate the approximate positions of the capsules at these times. Blue curve indicates the forces that are simply due to the patterned stripe; red curve represents the sum of forces due to the patterned stripe and due to the adhesion gradients created by the deposited nanoparticles.

on the capsules due to the blue patch (*i.e.*, determined from the parabolic decrease in energy imposed by this patch). The red curves reveal the total adhesive forces: the adhesive forces due to the modification of the surface by the nanoparticles and the adhesive forces due to the surface patterns. (Not shown in Fig. 5(b) and (c) is the fact that the red curves reach a minimum at approximately −0.8 at $x \approx 90$, where the curve increases rapidly towards zero.) Positive values of $F_x^{adh}$ correspond to a force that acts in the direction of the capsules' motion and thus propels the capsules forward along the stripe. Negative values of the force act in the reverse direction and thus, counteract the forward motion.

As can be seen in Fig. 5(b), at the interface between the green and blue patches (marked by the arrow), the net force acting on the leading edge of the cargo (target capsule closest to the triad) is negative, *i.e.*, the force acts to arrest the motion of this capsule. In this case, each of the neighboring cargo capsules experience a net positive force and the sum of the forces acting on each cargo capsule is slightly positive. Consequently, the entire cargo moves slightly forward so that the second target in the cargo feels the influence of the blue patch; hence, the magnitude of the net force acting on this target decreases, as seen in Fig. 5(c). Ultimately, the contributions from the neighboring cargo capsules are not sufficient to overcome the negative forces on the leading targets. As a result, the cargo comes to a stop (a few time steps after the image in Fig. 5(c)).

On the other hand, the net force on each target in the triad is positive (see Fig. 5(b) and (c)) since the "propelling" forces due to the modification of the surface by the nanoparticles dominate the "arresting" forces due to the capsules' interactions with the patches. While the force acting on the signaling capsule is negative at these time steps, the total force on the triad is positive due to the contributions from the two target capsules. In effect, the two targets in the triad "push" the signaling capsule forward and past the blue patch. (The signaling capsule feels this effective push through the surrounding fluid and thus, hydrodynamic interactions play an integral role in propelling the capsules along the adhesion gradient.[5,7])

The phase map in Fig. 6 reveals how the relative adhesive strengths of the blue and green domains affect the behavior of the system. When the strengths of adhesion between the target capsules and both the green and blue stripes ($\varepsilon_g^t$ and $\varepsilon_b^t$, respectively) are relatively low, the train approaches the blue patch. The four-target cargo remains localized at this location and then, the triad keeps moving along the path (Fig. 4(c)). The region of

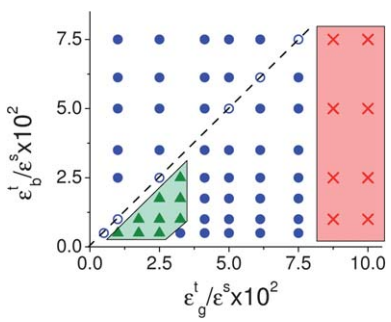


**Fig. 6** Phase map depicting the different regimes for the motion of a microcapsule train (triad and cargo). Green region: a triad drops off the cargo at the blue patch and then continues its movement. Filled blue circles: entire train stops at the blue patch. Open blue circles: the whole train passes the patch and continues moving. Red region: the moving train comes to a halt after it forms, before reaching the blue patch.

the parameter space where this behavior occurs is shaped light green in the phase map. At higher adhesions strengths (blue circles on the map), the entire train reaches the blue patch and stops at the position shown in Fig. 4(b). When $\varepsilon_g^t = \varepsilon_b^t$, the adhesion at the blue and green paths is equal, and therefore the adhesion gradient at the green–blue interface is zero; hence, the entire train passes the blue part and keeps moving along the stripe. (The open blue circles indicate the latter behavior in the phase map.) In the region shaded in red, a train eventually stops at an intermediate position due to high adhesion at the stripe, without reaching the blue patch.

The phase map indicates that there is an optimal range of adhesion strengths for the triad to perform as a pick-up and deliver micro-machine. It is important to note that these adhesion strengths can be achieved not only by tailoring the patches on the surface, but also by functionalizing the microcapsules. The fact that the surface of the microcapsules can be functionalized with a range of ligands expands the repertoire of materials that can be used to experimentally realize the above system.

## IV. Relevant experimental studies

Before concluding, we note that there are a number of experimental and computational studies indicating that many of the necessary components are in place for creating the active assemblies described above. In particular, recent experiments[16] have demonstrated that chemicals in the solution can induce local variations in the environment around a microcapsule, and these local variations can be utilized to trigger the release of the encapsulated species. The specific experiments involve LbL capsules that contain corrosion inhibitors and are embedded in a film. When the corrosion process occurs in the film, it releases byproducts that alter the local pH. The permeability of the polyelectrolyte shells strongly depends on pH and when the pH is changed in the neighboring area, the capsule's shell opens to release the inhibitor. Then, the released inhibitor suppresses the corrosion activity, and, the original pH value is restored, causing the capsules shell to close. This responsiveness of the capsules to local variations and the subsequent triggered release of the encapsulated species inspired our formulation of the role of the agonists and antagonists.

There is also experimental evidence that once the nanoparticles are released from the microcapsules, they could modify the capsule–surface interactions. In particular, experiments have also shown that a small fraction of nanoparticles adsorbed on a surface can significantly alter the adhesive interaction between microscopic colloids and this surface.[48] In the latter experiments, the bound nanoparticles made the surface effectively "stickier" for the microscopic colloids (and thus, could retard and even arrest the fluid-driven motion of the colloids over the surface). Based on these studies, one could potentially design an experiment where the bound nanoparticles would make the surface less adhesive for the capsules. Specifically, the underlying substrate could be coated with ligands that are attracted to functional groups distributed sparsely on the surface of the microcapsules or polymersomes.[11] The encapsulated nanoparticles would be tailored to encompass a higher surface coverage of the same functional groups that are on the microcapsules. Consequently, when these nanoparticles are released and diffuse near the surface, the ligands on the substrate would preferentially bind to the more functionalized (*i.e.*, effectively more attractive) nanoparticles and release their hold on the loosely bound microcapsules. In this manner the nanoparticles could make the surface less sticky for the microcapsules (as is the case considered here).

Our study is also inspired by experiments on the self-propelled motion of surfactant-filled, aqueous droplets on an adhesive surface.[49,50] The surfactants within a droplet adsorbed onto the surface with their hydrophilic heads, exposing their hydrophobic tails and thereby creating a gradient in wettability on the surface. Due to this gradient, the droplet underwent spontaneous motion away from the adsorbed surfactants.

While to date there have been no comparable experiments to demonstrate the spontaneous motion of microcapsules or polymersomes on adhesion gradients, there have, however, been both theoretical[51–54] and experimental studies[47] on the spontaneous movement of micron-sized vesicles due to gradients. In particular, Misbah and co-workers[51–54] have performed analytical calculations to pinpoint the conditions where adhesion gradients can lead to vesicle propulsion, or haptotaxis. Recently, Solon *et al.* have synthesized giant unilamellar vesicles (GUVs) that undergo self-induced haptotactic motion due to a charge gradient on the surface of a lipid bilayer.[47]

In our prior theoretical and computational studies,[18] we did predict that microcapsules can undergo spontaneous motion along an adhesion gradient, which was chemically patterned into the surface. In the latter studies,[18] we derived a scaling argument for the forces acting on a rigid microcapsule due to the gradient and thereby calculated the velocity of the capsule along the surface. We performed computer simulations on the same system[18] and found quantitative agreement between the scaling theory and these simulations. We also examined the motion of microcapsules on adhesion gradients that were created by released nanoparticles, which adsorbed onto the surface;[4–6] the capsules moved from the less adhesive to the more adhesive regions of the surface, *i.e.*, from regions of higher to lower nanoparticle coverage.[4,5] The latter behavior is reminiscent of experiments on the self-propelled droplets noted above.[47] Taken together, these theoretical calculations,[18,51–54] simulations[4–6] and experiments[49,50] provide strong indications that micron-sized capsules could undergo spontaneous motion on an adhesion gradient.

## V. Conclusions

In conclusion, we exploited the self-propelled motion of a system of microcapsules to ferry a cargo along a patterned surface in a fluid-filled chamber. The capsules in our system undergo haptotaxis, moving in response to an adhesion gradient on the surface. These capsules, however, create their own adhesion gradients as they emit the agonist and antagonist nanoparticles, which bind to the substrate. Hence, even in the absence of the green swath on the surface, these capsules undergo self-induced haptotaxis. The green stripe helps guide their motion so that the capsules travel to a specified location.

The positive and negative feedback introduced by the agonist and antagonist are necessary for the concerted motion of the capsules. With agonist alone, the surface would simply become too sticky and once all the targets were attracted to the signaling

capsule, the motion would stop. The antagonist introduces the necessary regions of weaker adhesion that contribute to the sustained motion of the capsules. The agonists and antagonists also control the permeability of the capsules and enable a dynamic readjustment in the release rates of the nanoparticles. The latter self-adjustments contribute to the evolving adhesion gradients that are necessary for concerted motion.

As is clear from the above discussion, the mobility of these capsules occurs in the absence of any externally applied stimulus. Taking advantage of this autonomous behavior, we isolated conditions where a triad of mobile capsules could convey a cargo to a desired location and then move on to potentially transport other payloads. The capsules themselves constitute a useful cargo since they can encapsulate a range of chemicals. Once localized at a particular region, the arrested capsules can be controllably triggered to release these encapsulated species (*e.g.*, *via* light[55] or changes in pH[14–16]). The latter attribute can be used to carry out site-specific reactions or controlled, multi-staged reactions in the microfluidic devices.

## Acknowledgements

The authors gratefully acknowledge financial support from the DOE (for support of GVK) and ONR (for partial support of VVY).

## References

1 S. J. Ebbens and J. R. Howse, *Soft Matter*, 2010, **6**, 726–738.
2 D. B. Weibel, P. Garstecki, D. Ryan, W. R. Diluzio, M. Mayer, J. E. Seto and G. M. Whitesides, *Proc. Natl. Acad. Sci. U. S. A.*, 2005, **102**, 11963–11967.
3 Y. Hong, D. Velegol, N. Chaturvedi and A. Sen, *Phys. Chem. Chem. Phys.*, 2010, **12**, 1423–1435.
4 O. B. Usta, A. Alexeev, G. Zhu and A. C. Balazs, *ACS Nano*, 2008, **2**, 471–476.
5 A. Bhattacharya, O. B. Usta, V. V. Yashin and A. C. Balazs, *Langmuir*, 2009, **25**, 9644–9647.
6 A. Bhattacharya and A. C. Balazs, *Phys. Rev. E: Stat., Nonlinear, Soft Matter Phys.*, 2010, **82**, 021801.
7 G. V. Kolmakov, V. V. Yashin, S. P. Levitan and A. C. Balazs, *Proc. Natl. Acad. Sci. U. S. A.*, 2010, **107**, 12417–12422.
8 C. S. Peyratout and L. Dähne, *Angew. Chem., Int. Ed.*, 2004, **43**, 3762–3783.
9 B. M. Discher, Y. Y. Won, D. S. Ege, J. C. M. Lee, F. S. Bates, D. E. Discher and D. A. Hammer, *Science*, 1999, **284**, 1143–1146.
10 R. A. L. Jones, *Nat. Mater.*, 2004, **3**, 209–210.
11 D. A. Hammer, G. P. Robbins, J. B. Haun, J. J. Lin, W. Qi, L. A. Smith, P. P. Ghoroghchian, M. J. Therien and F. S. Bates, *Faraday Discuss.*, 2008, **139**, 129–141.
12 E. G. Bellomo, M. D. Wyrsta, L. Pakstis, D. J. Pochan and T. J. Deming, *Nat. Mater.*, 2004, **3**, 244–248.
13 Y. J. Ma, W. F. Dong, M. A. Hempenius, H. Mohwald and G. J. Vancso, *Nat. Mater.*, 2006, **5**, 724–729.
14 G. B. Sukhorukov, A. A. Antipov, A. Voigt, E. Donath and H. Mohwald, *Macromol. Rapid Commun.*, 2001, **22**, 44–46.
15 D. G. Shchukin, M. Zheludkevich, K. Yasakau, S. Lamaka, M. G. S. Ferreira and H. Mohwald, *Adv. Mater.*, 2006, **18**, 1672–1678.
16 M. L. Zheludkevich, D. G. Shchukin, K. A. Yasakau, H. Mohwald and M. G. S. Ferreira, *Chem. Mater.*, 2007, **19**, 402–411.
17 M. N. Artyomov, J. Das, M. Kardar and A. K. Chakraborty, *Proc. Natl. Acad. Sci. U. S. A.*, 2007, **104**, 18958–18963.
18 A. Alexeev and A. C. Balazs, *Soft Matter*, 2007, **3**, 1500–1505.
19 O. B. Usta, A. Alexeev and A. C. Balazs, *Langmuir*, 2007, **23**, 10887–10890.
20 A. Alexeev, R. Verberg and A. C. Balazs, *Langmuir*, 2007, **23**, 983–987.
21 G. A. Buxton, C. M. Care and D. J. Cleaver, *Modell. Simul. Mater. Sci. Eng.*, 2001, **9**, 485–497.
22 A. J. C. Ladd, J. H. Kinney and T. M. Breunig, *Phys. Rev. E: Stat. Phys., Plasmas, Fluids, Relat. Interdiscip. Top.*, 1997, **55**, 3271–3275.
23 S. Succi, *The Lattice Boltzmann Equation for Fluid Dynamics and Beyond*, Clarendon Press, Oxford, UK, 2001.
24 A. Alexeev, R. Verberg and A. C. Balazs, *Macromolecules*, 2005, **38**, 10244–10260.
25 A. Alexeev, R. Verberg and A. C. Balazs, *Phys. Rev. Lett.*, 2006, **96**, 148103.
26 G. A. Buxton, R. Verberg, D. Jasnow and A. C. Balazs, *Phys. Rev. E: Stat., Nonlinear, Soft Matter Phys.*, 2005, **71**, 056707.
27 P. Lallemand and L. S. Luo, *Phys. Rev. E: Stat. Phys., Plasmas, Fluids, Relat. Interdiscip. Top.*, 2000, **61**, 6546–6562.
28 R. Verberg, A. Alexeev and A. C. Balazs, *J. Chem. Phys.*, 2006, **125**, 224712.
29 R. Verberg, A. T. Dale, P. Kumar, A. Alexeev and A. C. Balazs, *J. R. Soc., Interface*, 2007, **4**, 349–357.
30 R. Verberg, J. M. Yeomans and A. C. Balazs, *J. Chem. Phys.*, 2005, **123**, 224706.
31 H. C. Ottinger, *Stochastic Processes in Polymeric Fluids*, Springer, Berlin, 1996.
32 P. Szymczak and A. J. C. Ladd, *Phys. Rev. E: Stat., Nonlinear, Soft Matter Phys.*, 2003, **68**, 036704.
33 K. C. Chang and D. A. Hammer, *Biophys. J.*, 2000, **79**, 1891–1902.
34 E. F. Krasik, K. L. Yee and D. A. Hammer, *Biophys. J.*, 2006, **91**, 1145–1155.
35 A. Fery, F. Dubreuil and H. Mohwald, *New J. Phys.*, 2004, **6**, 18.
36 F. Dubreuil, N. Elsner and A. Fery, *Eur. Phys. J. E: Soft Matter Biol. Phys.*, 2003, **12**, 215–221.
37 N. Elsner, F. Dubreuil, R. Weinkamer, M. Wasicek, F. D. Fischer and A. Fery, *Prog. Colloid Polym. Sci.*, 2006, **132**, 117–123.
38 J. Heuvingh, M. Zappa and A. Fery, *Langmuir*, 2005, **21**, 3165–3171.
39 R. Mueller, K. Kohler, R. Weinkamer, G. Sukhorukov and A. Fery, *Macromolecules*, 2005, **38**, 9766–9771.
40 H. A. Stone, A. D. Stroock and A. Ajdari, *Annu. Rev. Fluid Mech.*, 2004, **36**, 381–411.
41 E. F. Krasik and D. A. Hammer, *Biophys. J.*, 2004, **87**, 2919–2930.
42 C. Dong, J. Cao, E. J. Struble and H. H. Lipowsky, *Ann. Biomed. Eng.*, 1999, **27**, 298–312.
43 S. Jadhav, C. D. Eggleton and K. Konstantopoulos, *Biophys. J.*, 2005, **88**, 96–104.
44 C. A. Chung and C.-Y. Chen, *J. Theor. Biol.*, 2009, **261**, 610–625.
45 R. T. Tranquillo, S. H. Zigmond and D. A. Lauffenburger, *Cell Motil. Cytoskeleton*, 1988, **11**, 1–15.
46 G. Maheshwari and D. A. Lauffenburger, *Microsc. Res. Tech.*, 1998, **43**, 358–368.
47 J. Solon, P. Streicher, R. Richter, F. Brochard-Wyart and P. Bassereau, *Proc. Natl. Acad. Sci. U. S. A.*, 2006, **103**, 12382–12387.
48 J. Zhang, S. Srivastava, R. Duffadar, J. M. Davis, V. M. Rotello and M. M. Santore, *Langmuir*, 2008, **24**, 6404–6408.
49 S. W. Lee, D. Y. Kwok and P. E. Laibinis, *Phys. Rev. E: Stat.,Nonlinear, Soft Matter Phys.*, 2002, **65**, 051602.
50 D. F. Dossantos and T. Ondarcuhu, *Phys. Rev. Lett.*, 1995, **75**, 2972–2975.
51 I. Cantat, K. Kassner and C. Misbah, *Eur. Phys. J. E: Soft Matter Biol. Phys.*, 2003, **10**, 175–189.
52 I. Cantat, C. Misbah and Y. Saito, *Eur. Phys. J. E: Soft Matter Biol. Phys.*, 2000, **3**, 403–412.
53 I. Cantat and C. Misbah, *Phys. Rev. Lett.*, 1999, **83**, 235–238.
54 I. Durand, P. Jonson, C. Misbah, A. Valance and K. Kassner, *Phys. Rev. E: Stat. Phys., Plasmas, Fluids, Relat. Interdiscip. Top.*, 1997, **56**, R3776–R3779.
55 M. F. Bedard, B. G. De Geest, A. G. Skirtach, H. Mohwald and G. B. Sukhorukov, *Adv. Colloid Interface Sci.*, 2010, **158**, 2–14.

 